Desalination and Water Treatment
www.deswater.com

doi: 10.5004/dwt.2023.29446

289 (2023) 180–190
March

Promoted adsorption performance for sulfide over CuO loaded hydrotalcite

Xinyang Huang[a], Lifang Hu[a,b,*], Jichao Zhu[a], Jihong Xu[a], Jie He[a], Xiaoyang Chen[c,*]

[a]*School of Chemical Engineering, Anhui University of Science and Technology, Huainan 232001, China, emails: hulf@aust.edu.cn (L. Hu), 1011342707@qq.com (X. Huang), zhujichao@aust.edu.cn (J. Zhu), ahlgxjh@sina.com (J. Xu), jiehe86@aliyun.com (J. He)*
[b]*Institute of Environment-Friendly Materials and Occupational Health, Anhui University of Science and Technology, Wuhu 241003, China*
[c]*School of Earth and Environment, Anhui University of Science and Technology, Huainan 232001, China, email: chenxy@aust.edu.c*

Received 1 October 2022; Accepted 1 March 2023

ABSTRACT

Sulfide is commonly found in wastewater from oil refining, petrochemical, pharmaceutical and other industries and must be removed because of its toxicity, odor and corrosiveness. In this research, the CuO loaded hydrotalcite adsorbent (CuO-HT) was prepared by the impregnation method. The as-prepared adsorbent was characterized by X-ray diffraction, scanning electron microscopy-mapping, X-ray photoelectron spectroscopy, Fourier-transform infrared spectroscopy and N_2 adsorption–desorption isotherms. The effect of CuO loading amount and calcination temperature on adsorption performance of industrial hydrotalcite for sulfide was examined in this experiment. The results reveal that the sulfide removal performance over CuO-HT is improvement. Among the as-prepared adsorbents, the hydrotalcite loaded with 5% Cu and calcined at 300°C (CuO-HT-5-300) had the highest removal rate of sulfide, and the removal rate is nearly 100% in 80 min. After four regenerated times, the adsorption rate of the adsorbent could still reach 90%. In the composite adsorbent, CuO was identified as the primary active element on the hydrotalcite carrier. The modified hydrotalcite had high sulfide adsorption capacity and excellent regeneration performance.

Keyword: Adsorption; Sulfide; Hydrotalcite; CuO

1. Introduction

Sulfur-containing wastewater will be discharged in industrial production, such as in medicine, paper, petrochemical, textiles and so on [1–3]. Sulfide in industrial sewage mainly exists in the form of compounds formed by metal ions and sulfur ions or hydrogen sulfide ions, including some non-metallic sulfides such as hydrogen sulfide and organic sulfides [4–6]. Sulfur-containing wastewater is highly corrosive and can even corrode modern buildings such as reinforced concrete [7,8]. When sulfur-containing wastewater enters farmland untreated, the roots of plants can rot, causing crops to wither and die. When the concentration of sulfide in water is 1.0~25.0 mg/L, freshwater fish will be died within 1~3 d [9,10]. When the concentration of sulfide in water continues to increase, volatile hydrogen sulfide gas is produced. Excessive inhalation will damage the human lung and central system, posing a threat to human life and health. Therefore, the treatment of sulfur-containing wastewater is imminent [11–13].

At present, there are many methods to remove sulfide and its by-products in sewage, such as chemical method [14], biological method [15], stripping method [16], precipitation method [17], advanced oxidation process (AOP) and so on [18]. However, most of these processes have the disadvantages of high cost, complicated process and easy generation of by-products [19–21]. The adsorption method is generally regarded as an economical and effective wastewater treatment method due to its advantages of simple operation, low price, strong selectivity, and difficulty in producing by-products [22,23].

* Corresponding authors.

Hydrotalcite is a layered hydroxide, whose structure is like brucite, and its chemical expression is $[M^{2+}_{1-x}M^{3+}_{x}(OH)_2]^{x+}[(A^{n-})_{x/n}\cdot mH_2O]^{x-}$, M^{2+} is divalent metal cation, M^{3+} is trivalent metal cation, x is the ratio of $M^{3+}/(M^{2+} + M^{3+})$, A^{n-} is the equilibrium anion between layers [24]. The anions between the aluminum hydroxide layers have certain mobility and ion exchange, and can be replaced by other anions in the environment. Due to its unique layered structure, anion exchange and "memory effect", hydrotalcite is widely used in sewage treatment, photoelectric catalysis, corrosion resistance and other fields [25,26].

In this study, industrial hydrotalcite was used as the carrier, Cu was loaded by impregnation method, and then calcined to prepare the modified hydrotalcite adsorbent. This adsorbent is used to adsorb and remove sulfides from water. Experimental variables included Cu loading amount and calcination conditions.

In addition, the properties of the adsorbents, including chemical and physical properties, were also discussed, characterized by X-ray diffraction (XRD), scanning electron microscopy (SEM-mapping), N_2 adsorption–desorption isotherms, X-ray photoelectron spectroscopy (XPS), and Fourier-transform infrared spectroscopy (FT-IR). According to the experimental results and characterization, the effects of loading and calcination temperature on the adsorption properties of hydrotalcite were determined, and the adsorption process was discussed.

2. Results and discussion

2.1. Adsorption performance of the adsorbents

2.1.1. Effect of Cu loading amount

The adsorption performance of hydrotalcite (HT) and CuO loaded hydrotalcite adsorbent (CuO-HT) with the different CuO loading amount (0%, 1%, 2%, 5% and 10%) for sulfide is illustrated in Fig. 1. From Fig. 1 it can be seen that HT has the weakest sorption performance for sulfides in water at only about 5% for the same sorption time. In contrast, the CuO-HT-5-300 and CuO-HT-10-300 has a best adsorption performance, close to 100%.

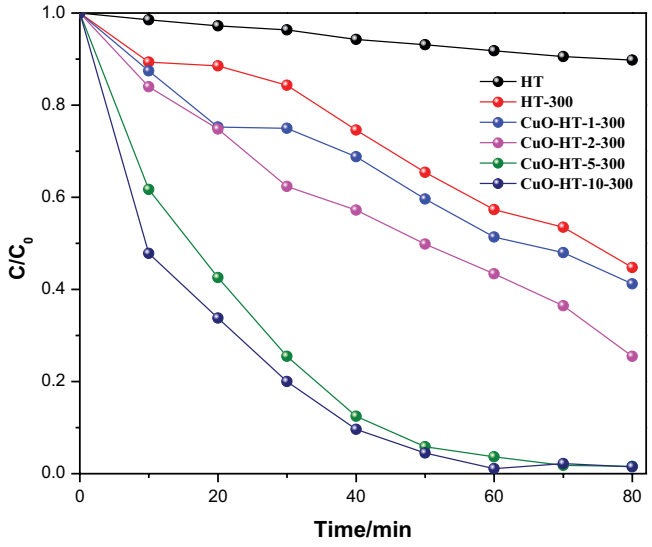

Fig. 1. Adsorption performance of CuO-HT adsorbents with the different CuO loading.

When the CuO loading was the variety of 1%–5%, the adsorption performance was positively linked with the loading. When the CuO loading was raised to 10%, the adsorption performance for sulfide was almost unchanged. This may be because the excess CuO accumulates itself and limits the exposure of some active sites.

Throughout the previous several decades, the kinetics equilibrium principle has been frequently utilized to the removal of contaminants from aqueous solutions [27]. To fit adsorption kinetic data, the quasi-first-order kinetic model was applied. The linear form of pseudo-first-order equation was expressed as:

$$\ln\left(\frac{C_0}{C}\right) = k \cdot t \tag{1}$$

where C and C_0 represent the concentration of sulfide solution in the reaction device when the adsorption time is t and t_0 (t = 0), respectively, and k is the rate constant of the first order kinetic reaction [28].

It can be seen from Fig. 2a that the reaction conforms to the pseudo-first-order kinetic formula. According to Fig. 2b, the k value of the fitting curve increases with the increase of loading capacity, representing the improvement of adsorption performance. According to the kinetic curve, the k value of CuO-HT-5-300 is almost equivalent to that of CuO-HT-5-300. In addition, from the perspective of economy, CuO-HT-5-300 is the best choice for the adsorption of sulfide.

2.1.2. Effect of calcination temperature

The effects of calcination temperature on the adsorption performance of HT and CuO-HT are investigated, and the findings are illustrated in Figs. 4 and 5.

Fig. 3 shows the adsorption performance of HT for sulfide at different calcination temperatures (100°C, 200°C, 300°C, 400°C, 500°C). The result shows that HT-300 has the best adsorption performance, and the adsorption performance is positively correlated with the calcination temperature at the range of 95°C to 300°C. When the calcination temperature reaches 400°C, the adsorption performance of sulfide was reduced.

The calcination temperature of the adsorbent is a critical determinant of adsorption performance throughout the preparation process. Appropriate calcination temperature can improve the adsorption ability of adsorbent. The calcination temperature has a significant effect on the morphology, pore structure, crystallinity, and specific surface area of the adsorbent. Fig. 4 shows the effect of calcination temperature of CuO-HT-5-y on the adsorption performance for the sulfide. The CuO-HT-5-300 has the best adsorption performance.

When the calcination temperature reaches 170°C, the $Cu(NO_3)_2$ starts to decompose CuO. Therefore, when the temperature is less than 170°C, the CuO cannot be generated as active catalysis point and the CuO-HT has a poor adsorption performance of sulfide. Over 170°C, the CuO can be

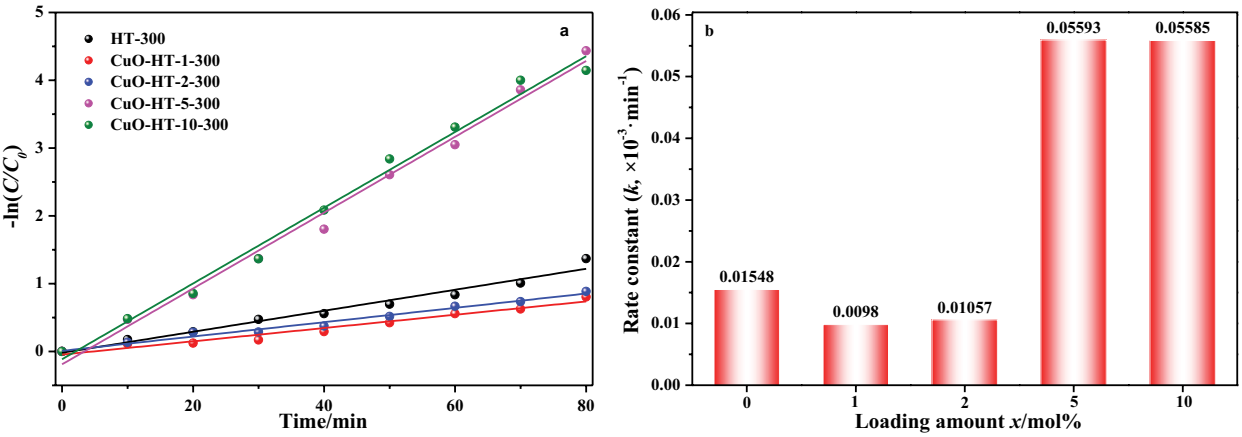

Fig. 2. Pseudo-first-order curves of CuO-HT-*x*-300 with different loading amount (a) and the reaction rate constant *k* (b).

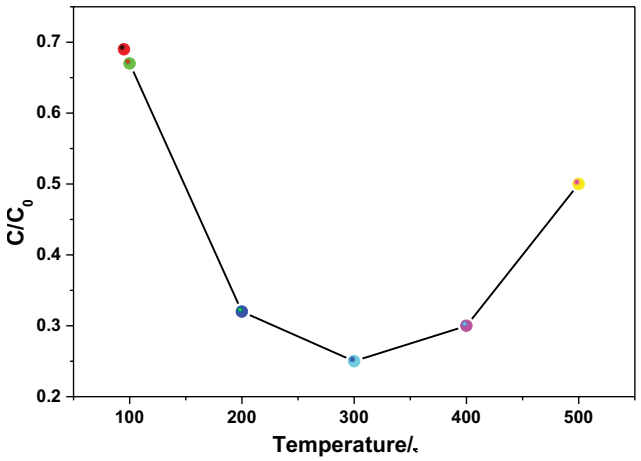

Fig. 3. Adsorption performance of HT for sulfide with different calcination temperatures.

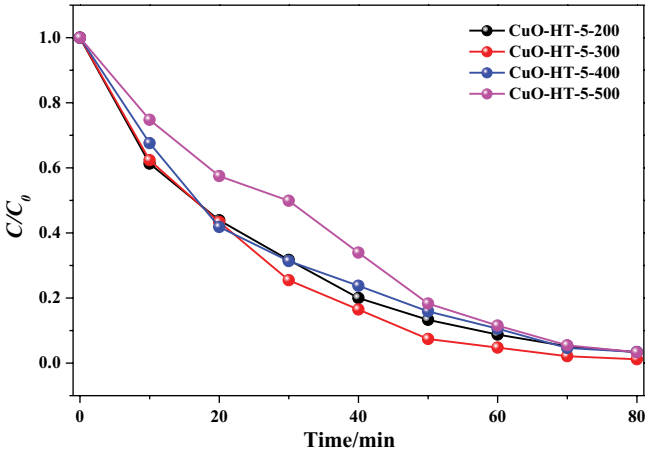

Fig. 4. Adsorption performance of CuO-HT-5-*y* for sulfide with different calcination temperatures.

formed as the active component, but cannot easily diffused to equilibrium on the carrier surface. This makes the catalytic activity cannot be fully played, result in a low adsorption performance of Na_2S. When the calcination temperature was over 400°C, the removal rate of Na_2S was decreased. The high calcination temperature cause sintering of adsorbent, larger crystalline grain and reduced surface area, lead to the decrease of adsorbent activity. In summary, HT and CuO-HT has the best performance after calcination at 300°C.

To evaluate the adsorption performance of various samples even further, the relevant sulfide adsorption data of different adsorbents were analyzed by kinetics.

It can be seen from Fig. 5 that the adsorption process of different adsorbents conforms to the pseudo-first-order kinetic equation. Fig. 5a shows that when the calcination temperature is in the interval of 200°C–300°C, the rate constant *k* of the first-order kinetic curve increases gradually, show that the reaction rate keeps increasing. The rate constant of 300°C is very close to that of 400°C. After calcination at 300°C–500°C, HT has a unique memory effect [29], although HT laminate presented different degree of collapse, but the layer structure still exists. After contact with water, it can also be restored to its original ordered layered structure, which leads to a promoted adsorption capacity. However, when the calcination temperature of samples was 500°C, the lamellar structure has been destroyed and the spinel structure was formed. Additionally, the surface area and pore volume are being reduced, resulting in a drop-in adsorption capacity [30].

Combined with the experimental results, it can be proved that the preparation method of calcination modified HT by impregnation of support metal ions is simple to operate, economical and practical. And it is a promising adsorbent capable of adsorbing sulfides from wastewater. When the loading amount is 5% and the calcination temperature is 300°C, the sulfide adsorbent capacity of the adsorbent is the best. Within 80 min, the adsorption capacity of sulfide reaches nearly 100%, and the adsorption rate is relatively rapid. The regeneration performance of the adsorbent needs further discussed.

2.2. Characterization of the as-prepared adsorbents

According to the above analysis results, CuO-HT-5-300 has the highest adsorption performance for sulfide. In this

study, CuO-HT-5-300 was selected and used HT and HT-300 as a reference to characterize and analyze.

The morphology and elemental distribution of CuO-HT-5-300 were characterized by SEM and elemental mapping, and the results are shown in Fig. 6. After calcination, the sheet-like structure of HT was collapsed but became more densely packed. The presence of Cu in the CuO-HT-5-300 was detected by elemental mapping, but the amount of Cu was small.

The effect of loaded CuO on structure of HT is described by XRD and N_2 adsorption–desorption isotherm. The results are shown in Figs. 8 and 9.

Fig. 7 shows the XRD patterns of the HT, HT-300, CuO-HT-5-300 and CuO-HT-10-300. As showed in Fig. 7a, the XRD pattern of HT is keep high consistency with the standard card of PDF#89-0460 in the inorganic crystal database. This indicated that HT has a high crystallinity and a distinct lamellar structure. The peaks at 2θ values of 11.7° and 23.5° are attributed to the (003) and (006) in HT [31,32], which indicate that the layered structure of HT is obvious. After calcination, the strength of the (003) distinctive diffraction peak drops progressively and formed a low intensity diffraction peak with a large peak width. Meanwhile, the 2θ values of (003) characteristic diffraction peak gradually offset to a large angle, and the (006) characteristic diffraction peaks disappeared. According to the standard diffraction pattern of MgO (PDF# 45-0946), the characteristic diffraction peak of MgO at the 2θ values of 60.7° is observed in Fig. 8b–d. These illustrated that the layer board

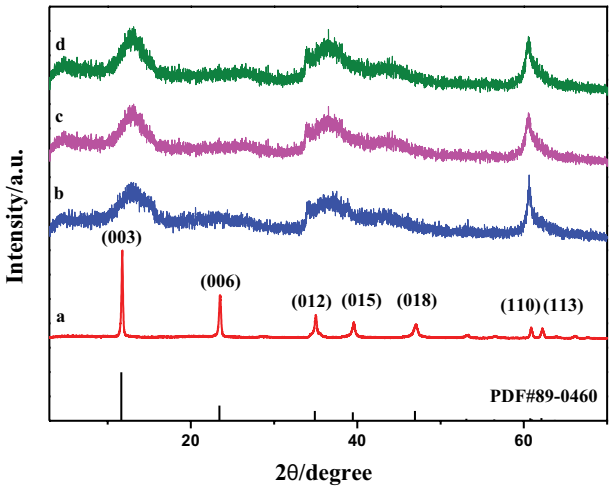

Fig. 7. X-ray diffraction patterns of HT (a), HT-300 (b), CuO-HT-5-300 (c) and CuO-HT-10-300 (d).

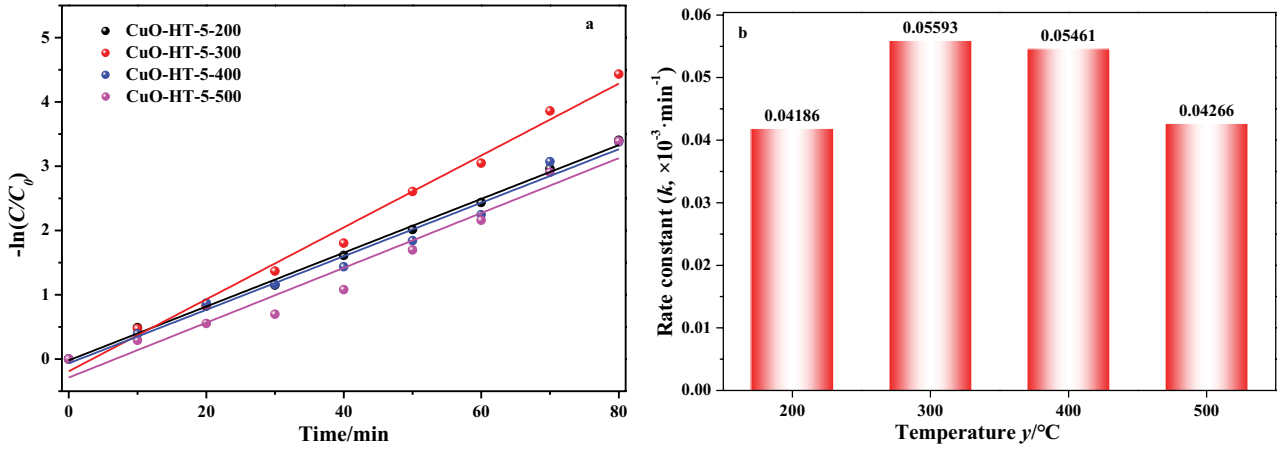

Fig. 5. Pseudo-first-order kinetic curves of CuO-HT-5-*y* with different calcination temperatures (a), and the reaction rate constant *k* (b).

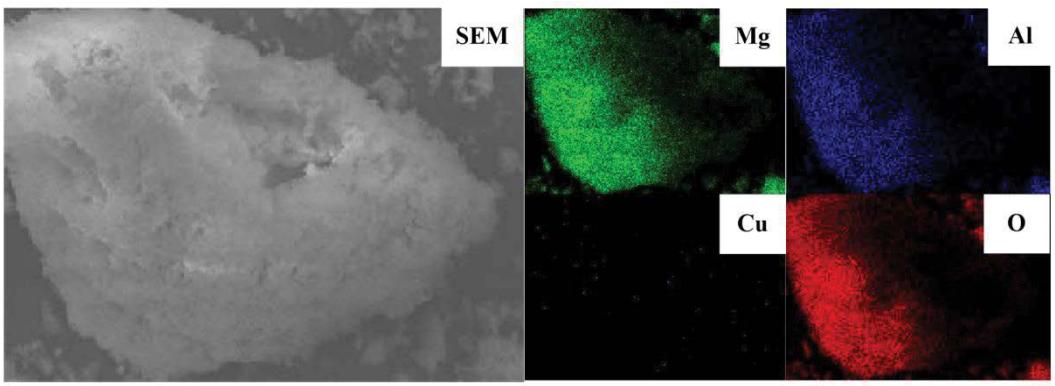

Fig. 6. Scanning electron microscopy images and elemental mapping of CuO-HT-5-300.

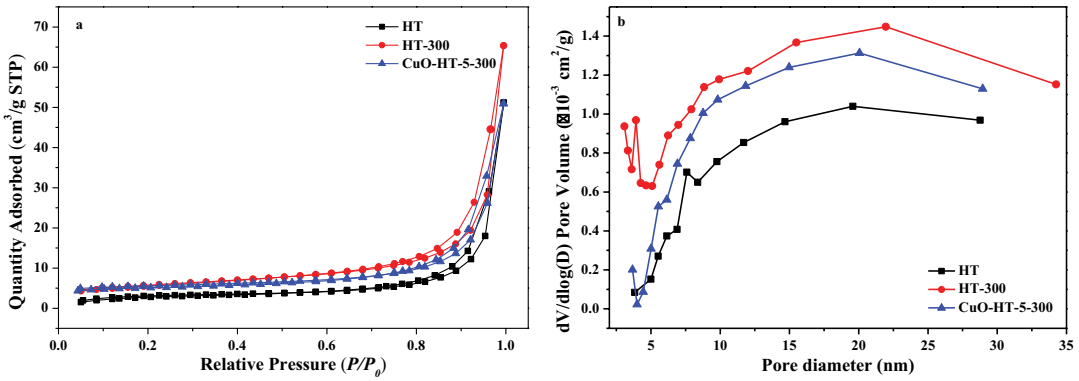

Fig. 8. N_2 adsorption–desorption curve (a) and pore-size distribution (b) of HT, HT-300 and CuO-HT-5-300.

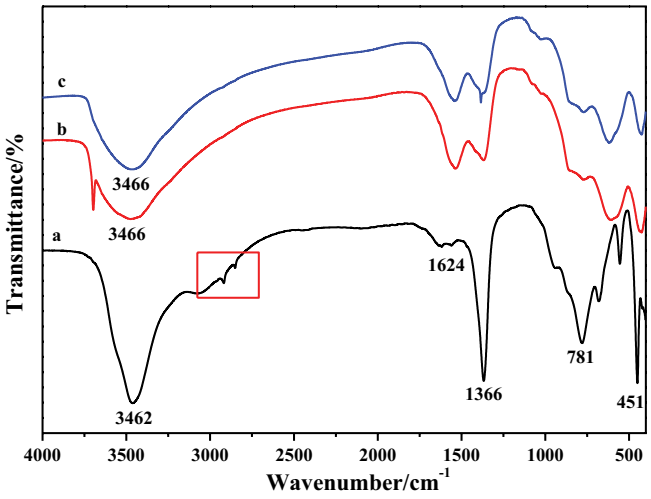

Fig. 9. Fourier-transform infrared spectroscopy of HT (a), HT-300 (b) and CuO-HT-5-300 (c).

structure of HT was partially destroyed after calcination at 300°C for 3 h [33]. Compared with HT-300, the XRD pattern of CuO-HT-5-300 and CuO-HT-10-300 has no obvious change, indicating that the loading process has no effect on the structure of HT-300. In addition, there was no characteristic peak of CuO in the XRD pattern of CuO-HT-5-300 and CuO-HT-10-300. Combined with SEM-mapping, it showed that CuO was evenly dispersed on the surface of HT.

The N_2 adsorption and desorption isotherm measurement was used to analyzed the surface area and the distribution of pores in the samples that had been produced. As illustrated in Fig. 8a, the adsorption isotherms of the as-prepared samples are all IV types and the H_3 hysteresis loop (IUPAC classification), indicating that the HT congregate and stack to produce slit-like gaps. The pore-size distribution curve produced utilizing adsorption branch data using the Barrett–Joyner–Halenda method shows that all of the pore sizes of the as-prepared samples are in the range of 2–35 nm, indicating a mesoporous structure [34]. It is belong to porous adsorbent, therefore, the phenomenon of capillary coalescence appears, so it has a strong interaction with the adsorbent [35]. The pore-size distribution of HT is mainly aggregated at 7.6 nm. After calcinated, the

Table 1
Some parameters of HT, HT-300 and CuO-HT-5-300

Samples	S_{BET} (m^2/g)	V_{total} (cm^3/g)
HT	11.74	0.03
HT-300	20.14	0.05
CuO-HT-5-300	18.64	0.04

pore-size distribution was more dispersed for HT-300 and CuO-HT-5-300. It indicated that the layer board structure of HT was destroyed. Moreover, the specific surface area and pore volume of HT-300 and CuO-HT-5-300 are larger than those of HT (Table 1). Large specific surface area and pore volume enable Na_2S to interact with adsorption active sites in HT, in the meantime decreasing the steric hindrance effect. This is consistent with XRD results. Enhancing these qualities is critical for optimizing its adsorption efficacy.

As seen in Fig. 9, the FT-IR characterizations were utilized to investigate the surface functional groups of the various samples. These spectra are similar to those previously reported for hydrotalcites in the literature [36]. As illustrated in Fig. 9a, at 3,462; 1,624; 1,366 and 781 cm^{-1}, four significant peaks are assigned. The fundamental stretching and bending vibrations of H_2O or hydroxyl group can be attributed to the peaks located at 3,462 and 1,624 cm^{-1}, respectively [37]. The peak located at 1,366 cm^{-1} is attributed to the stretching vibration CO_3^{2-} [38]. Between 800 and 500 cm^{-1}, the bands correspond to the M–O and M–O–M vibrations of the hydroxide layer (M = Al, Mg) [39]. The peak near 2,900 cm^{-1} is the organic impurity in the industrial HT. Fig. 9b and c are the FT-IR of HT-300 and CuO-HT-5-300, respectively. After being calcined, the peak located at 3,462 and 1,366 cm^{-1} became weakness. It could be after calcination, H_2O was removed and CO_3^{2-} overflows in the form of CO_2. The peak located at 1,624 cm^{-1} was observed become stronger. These indicate that the layered structure of HT was destroyed by calcination, and the group of CO_3^{2-} existing between the layers was disintegrated. After Cu loading, the characteristic peaks of Al–O bond and Mg–O bond at 774 and 613 cm^{-1} in FT-IR of HT-300 were moved slightly, which may be caused by CuO load. In addition, the shift amplitude of the characteristic peak of Mg–O is greater than that of Al–O, indicating that CuO mainly interacts with Mg–O during loading.

Further interaction model between CuO and HT-300, and the surface element states of CuO-HT-5-300 were characterized by XPS, and the results are shown in Fig. 10.

As shown in XPS spectrum of CuO-HT-5-300, the characteristic peaks of Cu 2p, Mg 1s, Al 2p and O 1s are appeared, in indicated that Cu was loaded on the surface of HT successfully. Fig. 10b shows the high-resolution spectrum of Cu 2p. The peaks at 955.5 and 935.3 eV are attributed to Cu $2p_{1/2}$ and Cu $2p_{3/2}$ of Cu^{2+}, and the peaks at 952.6 and 933.0 eV are corresponded to Cu $2p_{1/2}$ and Cu $2p_{3/2}$ of Cu^{+} [40,41]. It indicated that CuO/Cu_2O coexists on the HT surface after CuO loading. Compared with HT-300, in the XPS spectrum of CuO-HT-5-300, the characteristic peak of Al 2p did not change significantly, but the characteristic peaks of Mg 1s and O 1s moved significantly during the loading process. It shows that CuO has obvious interaction with Mg–O, which is consistent with the results of FT-IR.

2.3. Regeneration performance of the adsorbent

The results of the adsorption performance of regenerated CuO-HT-5-300 for sulfide are shown in Fig. 11. The adsorption rate of the adsorbent shown a declining trend, after four times adsorption–desorption cycle regeneration experiments, the adsorption performance of the worked CuO-HT-5-300 is 90%. It is slightly lower than that of the unworked CuO-HT-5-300. This may be because a small amount of sulfide is not effectively desorbed during the

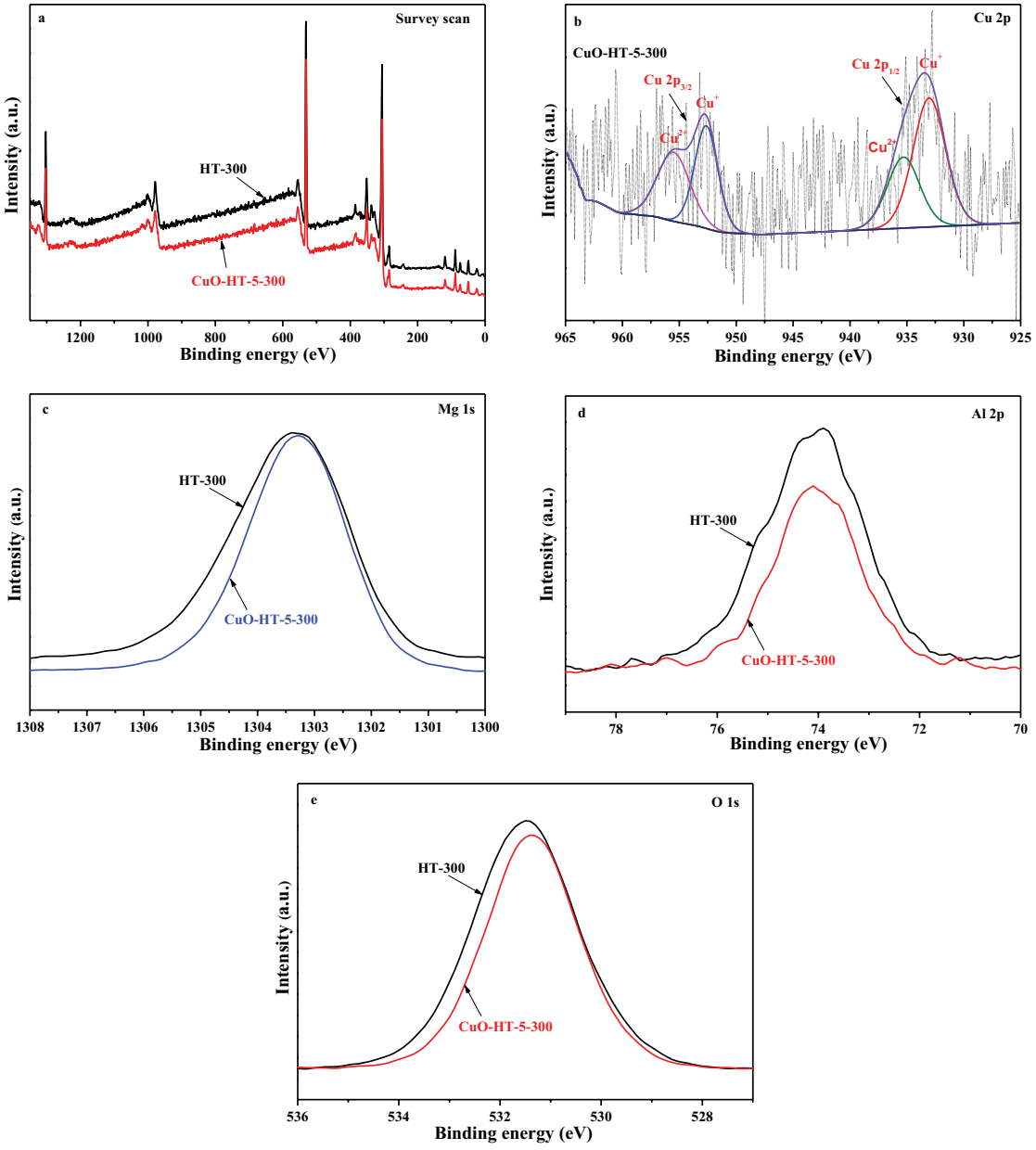

Fig. 10. X-ray photoelectron spectra of HT-300 and CuO-HT-5-300 survey scan (a), Cu 2p (b), Mg 1s (c), Al 2p (d) and O 1s (e).

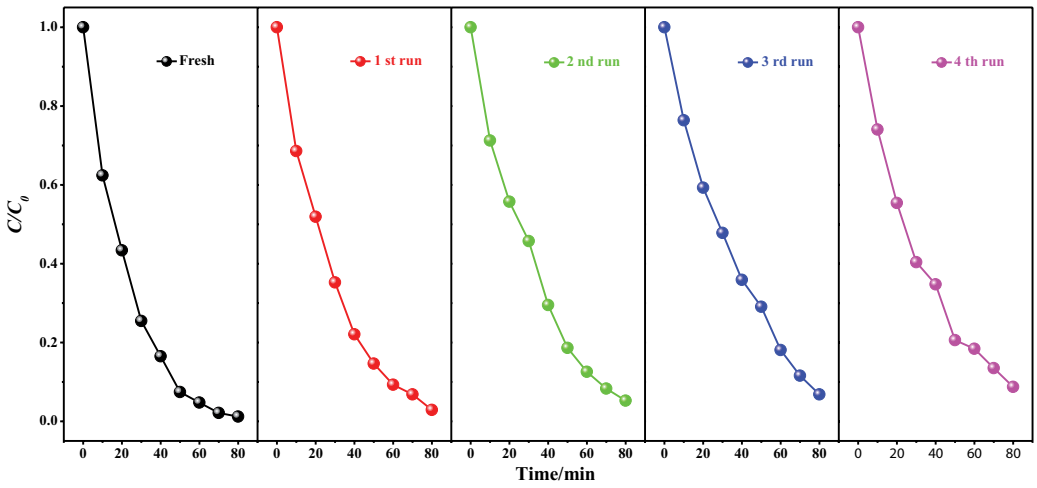

Fig. 11. Adsorption performance of regenerated CuO-HT-5-300 for sulfide.

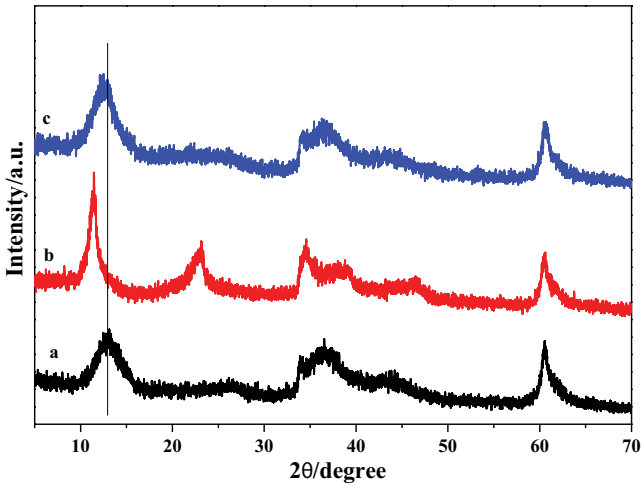

Fig. 12. X-ray diffraction patterns of unworked (a), worked (b) and regenerated (c) CuO-HT-5-300.

regeneration process, resulting in the occupation of part of the active site.

Fig. 12 shows the XRD patterns of the unworked, worked and regenerated CuO-HT-5-300, respectively. After adsorption of sulfide, the sharp and symmetric peaks at lower 2θ (003, 006) reappeared, suggesting that the sulfide was adsorbed onto the positive layer and formed the negative layer [42]. This indicated that he calcined HT recovered their original layered structure. Anion incorporation was occurred during the adsorption process. Which was ascribed to rehydration and structural reconstruction of the calcined products in the adsorption process of sulfide [43]. After regeneration, the XRD pattern is shown in Fig. 12c. The peak corresponding to (006) plane disappeared, comparison the peaks of unworked and regenerated CuO-HT-5-300, there are no significant change in XRD pattern. It indicated that the structure of the regenerated CuO-HT-5-300 was recovered well. Combined with regeneration adsorption rate, the sample has good regeneration performance.

2.4. Adsorption mechanism

The adsorption mechanism of CuO-HT-5-300 for sulfide was characterized by XPS, and the results are shown in Fig. 13. As shown in Fig. 13b, the characteristic peaks of S 2p are appeared, the peak located at 161.67 eV is assigned to the sulfide, and the other peak located at 168.58 eV is ascribed to the sulfate [44,45]. it indicated that the adsorption of sulfide by adsorbent was determined. Sulfide is volatile. The adsorbed sulfide is largely desorbed during the vacuum pumping process of XPS characterization, and all detected sulfides are less than those actually adsorbed. As shown in Fig. 13c–e, the characteristic peaks of Mg 1s, Al 2p and O 1s are hardly changed, this shows that sulfide is not adsorbed on the surface of Al–O and Mg–O. The relative content of Cu^{2+} in CuO-HT-5-300 before and after adsorption was analyzed. It was found that Cu^{2+} changed to Cu^{+} after adsorption, and its relative content decreased from 41% to 11%. It shows that Cu^{2+} as the main active site promotes the adsorption of sulfide via the Cu–S interaction in the adsorption process.

3. Conclusion

CuO-HT was successfully prepared by impregnation and high temperature calcination. The results of the physicochemical characterizations of the CuO-HT material showed that CuO were successfully loaded on HT. Moreover, the adsorption performance of CuO-HT for sulfide in sewage is significantly improved. The adsorption performance of CuO-HT-5-300 is highest with nearly 100% in roughly 80 min. The regenerated adsorbent obtained after washing by dilute nitric acid and calcination also has good adsorption performance, and the adsorption performance for sulfide is still over 90% after four times of regeneration. In the composite, Cu^{2+} is the main active site to promote the adsorption of sulfide via the Cu–S interaction in the adsorption process. The current research will promote the development of highly efficient adsorbents combining metal oxides and hydrotalcite to improve the adsorption performance for sulfide.

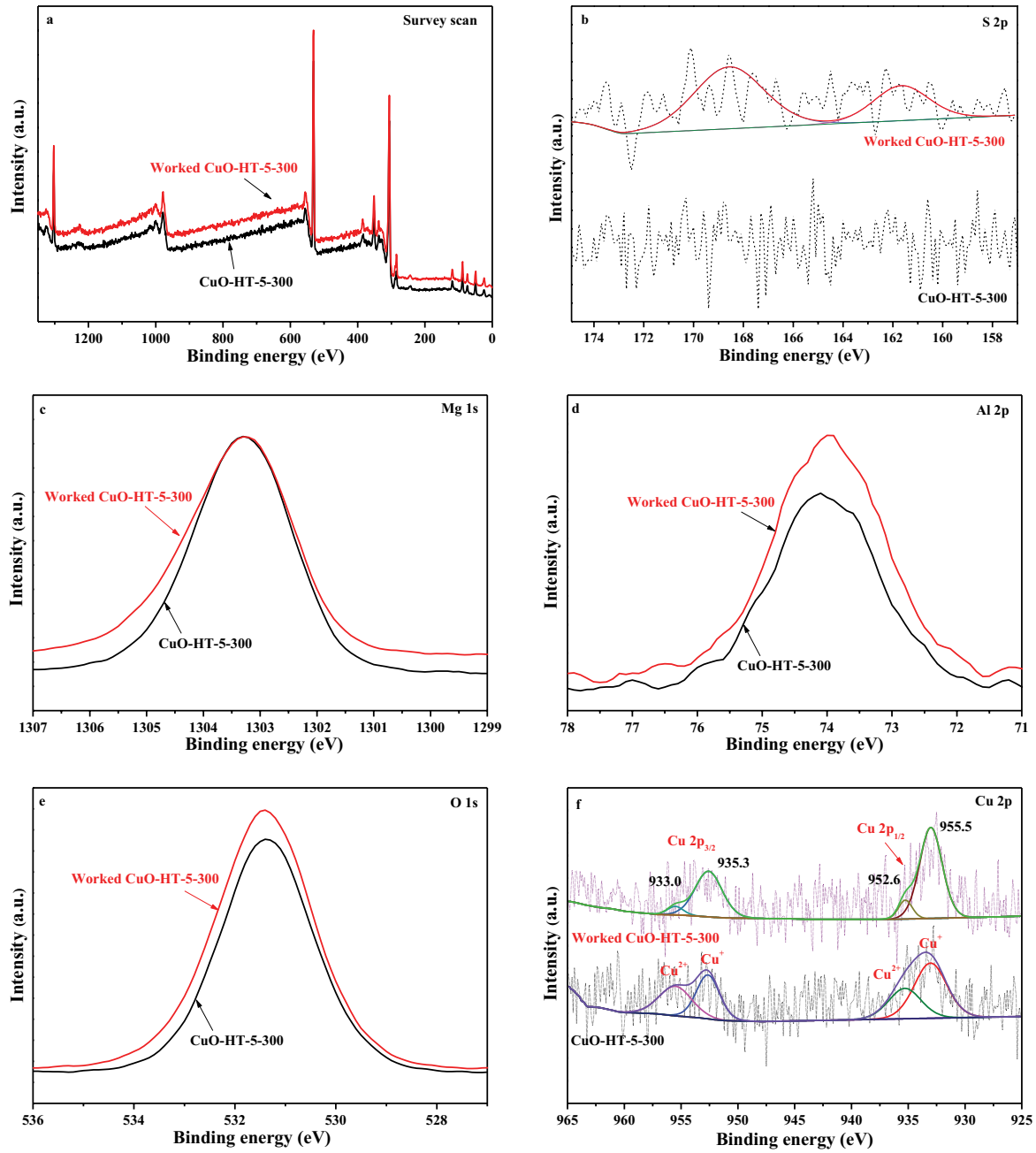

Fig. 13. X-ray photoelectron spectra of CuO-HT-5-300 and worked CuO-HT-5-300 survey scan (a), S 2p (b), Mg 1s (c), Al 2p (d), O 1s (e) and Cu 2p (f).

Data availability

No data was used for the research described in the article.

Acknowledgements

This work was supported by the Research Foundation of the Institute of Environment-friendly Materials and Occupational Health of Anhui University of Science and Technology (Wuhu) [No. ALW2020YF09] and Innovation Fund Project of Anhui University of Science and Technology Graduate [No. 2021CX2098].

CRediT authorship contribution statement

All authors contributed to the study conception and design. Xinyang Huang: Experiments, Characterization, Data analysis, Writing–original draft. Lifang Hu: Investigation, Methodology, Supervision, Conceptualization, Data curation, Formal analysis, Writing–review and editing. Jichao Zhu: Data analysis, Investigation. Jihong Xu: Validation, Writing–review & editing. Jie He: Data analysis, Writing–review and editing. Xiaoyang Chen: Supervision, Writing–review and editing.

Declaration of competing interest

The authors declare that they have no known competing financial interests or personal relationships that could have appeared to influence the work reported in this paper.

References

[1] Z. Xia, X. Peng, L. Kong, X. Hu, Hydrophilicity/hydrophobicity of metal sulfide particles as a determinator of aggregation performance in wastewater, J. Water Process Eng., 40 (2021) 101900, doi: 10.1016/j.jwpe.2020.101900.

[2] R.V. Matos, N. Matias, F. Ferreira, J.S. Silva, J.S. Matos, Assessment of sulfide production in a full scale wastewater sludge rising main, J. Environ. Manage., 209 (2018) 505–514.

[3] S. Giuliani, T. Zarra, V. Naddeo, V. Belgiorno, A novel tool for odor emission assessment in wastewater treatment plant, Desal. Water Treat., 55 (2015) 712–717.

[4] M.A. EI-Khateeb, E.H.A. Nashy, A.A.A. Nayl, Combining chemical coagulation process and innovative aerobic reactor for the treatment of de-hairing wastewater, Waste Biomass Valorization, 7 (2020) 2557–2564.

[5] J.M. Costa, K.C. Castro, R.P. Rodriguez, G.P. Sancinetti, Anaerobic reactors for the treatment of sulphate and metal-rich wastewater: a review, Int. J. Environ. Anal. Chem., 102 (2020) 923–934.

[6] A.F.R. Silva, B.C. Ricci, K. Koch, M. Weißbach, M.C.S. Amaral, Dissolved hydrogen sulfide removal from anaerobic bioreactor permeate by modified direct contact membrane distillation, Sep. Purif. Technol., 233 (2019) 116036, doi: 10.1016/j.seppur.2019.116036.

[7] X. Sun, G. Jiang, P.L. Bond, J. Keller, Periodic deprivation of gaseous hydrogen sulfide affects the activity of the concrete corrosion layer in sewers, Water Res., 157 (2019) 463–471.

[8] H. Hasler-Sheetal, M. Holmer, Sulfide intrusion and detoxification in the seagrass *Zostera marina*, PLoS One, 10 (2015) 0129136, doi: 10.1371/journal.pone.0129136.

[9] Q. Chi, D. Wang, X. Hu, S. Li, S. Li, Hydrogen sulfide gas exposure induces necroptosis and promotes inflammation through the MAPK/NF-κ B pathway in broiler spleen, Oxid. Med. Cell. Longevity, 2019 (2019) 1–13, doi: 10.1155/2019/8061823.

[10] Q. Xu, M. Liang, W. Xu, D. Huang, Advances in mechanism and influencing factors affecting hydrogen sulfide adsorption by biochar, Environ. Earth Sci., 42 (2021) 5086–5099.

[11] X. Lu, J. Li, H. Liu, W. Li, R. Wang, J. Lu, Microbial oxidation of metal sulfides and its consequences, Acta Petrol. Sin., 35 (2019) 153–163.

[12] T.J. Bandosz, On the adsorption/oxidation of hydrogen sulfide on activated carbons at ambient temperatures, J. Colloid Interface Sci., 246 (2002) 1–20.

[13] D. Liu, B. Li, J. Wu, Y. Liu, Sorbents for hydrogen sulfide capture from biogas at low temperature: a review, Environ. Chem. Lett., 18.1 (2020) 113–128.

[14] I. Anastopoulos, I. Pashalidis, A.G. Orfanos, I.D. Manariotis, T. Tatarchuk, L. Sellaoui, A. Bonilla-Petriciolet, A. Mittal, A. Núñez-Delgado, Removal of caffeine, nicotine and amoxicillin from (waste)waters by various adsorbents. A review, J. Environ. Manage., 261 (2020) 110236, doi: 10.1016/j.jenvman.2020.110236.

[15] R. Peighami, B. Rasekh, E. Motamedian, F. Yazdian, H. Khodaverdi, Investigating the ability of sulfur oxidizing strains in biodesulfurisation of sulfide-containing streams, screening the most capable strain and determining the optimum condition for elemental sulfur recovery from sulfide using response surface method, Fuel, 309 (2022) 121985, doi: 10.1016/j.fuel.2021.121985.

[16] R. Noorain, T. Kindaichi, N. Ozaki, Y. Aoi, A. Ohashi, Integrated biological-physical process for biogas purification effluent treatment, J. Environ. Sci., 83 (2019) 110–122.

[17] X. Zhang, J. Tian, Y. Hu, H. Han, X. Luo, W. Sun, T. Yue, L. Wang, X. Cao, H. Zhou, Selective sulfide precipitation of copper ions from arsenic wastewater using monoclinic pyrrhotite, Sci. Total Environ., 705 (2020) 135816, doi: 10.1016/j.scitotenv.2019.135816.

[18] D. Barki, S. Sabach, Y. Dubowski, Removal of chlorinated organic pollutants from groundwater using a vacuum-UV-based advanced oxidation process, ACS ES&T Water, 9 (2021) 2076–2086.

[19] P.F. Lito, J.P.S. Aniceto, C.M. Silva, Removal of anionic pollutants from waters and wastewaters and materials perspective for their selective sorption, Water Air Soil Pollut., 223 (2012) 6133–6155.

[20] V.S. Saji, Research advancements in sulfide scavengers for oil and gas sectors, Rev. Chem. Eng., 1 (1982) 2191–0235, doi: 10.1515/revce-2019-0049.

[21] K. Gaj, Applicability of selected methods and sorbents to simultaneous removal of siloxanes and other impurities from biogas, Clean Technol. Environ. Policy, 19 (2017) 2181–2189.

[22] S. Soni, P.K. Bajpai, J. Mittal, C. Arora, Utilisation of cobalt doped iron-based MOF for enhanced removal and recovery of methylene blue dye from wastewater, J. Mol. Liq., 314 (2020) 113642, doi: 10.1016/j.molliq.2020.113642.

[23] J. Mittal, V. Thakur, A. Mittal, Batch removal of hazardous azo dye Bismark Brown R using waste material hen feather, Ecol. Eng., 60 (2013) 249–253.

[24] Z. Tang, Z. Qiu, S. Lu, X. Shi, Functionalized layered double hydroxide applied to heavy metal ions absorption: a review, Nanotechnol. Rev., 9 (2020) 0065, doi: 10.1515/ntrev-2020-0065.

[25] W. Lv, J. Sun, Y. Yao, M. Du, Q. Zheng, Morphology control of layered double hydroxide and its application in water remediation, Prog. Chem., 32 (2020) 2049–2063.

[26] M. Zubair, I. Ihsanullah, H.A. Aziz, M.A. Ahmad, M.A. Al-Harthi, Sustainable wastewater treatment by biochar/layered double hydroxide composites: progress, challenges, and outlook, Bioresour. Technol., 319 (2020) 124128, doi: 10.1016/j.biortech.2020.124128.

[27] H. Yuh-Shan, Citation review of Lagergren kinetic rate equation on adsorption reactions, Scientometrics, 59 (2004) 171–177.

[28] Y.S. Ho, G. McKay, Sorption of dye from aqueous solution by peat, Chem. Eng. J., 70 (1998) 115–124.

[29] P. Wu, L. Xia, Y. Liu, J. Wu, Q. Chen, S. Song, Simultaneous sorption of arsenate and fluoride on calcined Mg-Fe-La hydrotalcite-like compound from water, ACS Sustainable Chem. Eng., 6 (2018)16287–16297.

[30] W. Ma, N.N. Zhao, G. Yang, L. Tian, R. Wang, Removal of fluoride ions from aqueous solution by the calcination product of Mg-Al-Fe hydrotalcite-like compound, Desalination, 268 (2011) 20–26.

[31] L.A. Ramírez-Llamas, R. Leyva-Ramos, A. Jacobo-Azuara, J.M. Martínez-Rosales, E.D. Isaacs-Paez, Adsorption of fluoride from aqueous solution on calcined and uncalcined layered double hydroxide, Adsorpt. Sci. Technol., 33 (2015) 393–410.

[32] A.A.A. Ahmed, Z.A. Talib, M.Z. Hussein, A. Zakaria, Improvement of the crystallinity and photocatalytic property of zinc oxide as calcination product of Zn-Al layered double hydroxide, J. Alloys Compd., 539 (2012) 154–160.

[33] D. Wan, H. Liu, R. Liu, J. Qu, S. Li, J. Zhang, Adsorption of nitrate and nitrite from aqueous solution onto calcined (Mg-Al) hydrotalcite of different Mg/Al ratio, Chem. Eng. J., 195–196 (2012) 241–247.

[34] M. Thommes, K. Kaneko, A.V. Neimark, J.P. Olivier, F. Rodriguez-Reinoso, J. Rouquerol, K.S.W. Sing, Physisorption of gases, with special reference to the evaluation of surface area and pore-size distribution (IUPAC Technical Report), Pure Appl. Chem., 87 (2016), doi: 10.1515/pac-2014-1117.

[35] B. Coasne, A. Grosman, C. Ortega, M. Simon, Adsorption in non-interconnected pores open at one or at both ends: a reconsideration of the origin of the hysteresis phenomenon, Phys. Rev. Lett., 88 (2002) 256102, doi: 10.1103/PhysRevLett.88.256102.

[36] J. Xie, N. Yan, S. Yang, Z. Qu, W. Chen, W. Zhang, K. Li, P. Liu, J. Jia, Synthesis and characterization of nano-sized Mn-TiO_2 catalysts and their application to removal of gaseous elemental mercury, Res. Chem. Intermed., 38 (2012) 2511–2522.

[37] X. Kong, Q. Lu, J. Huang, L. Li, J. Zhang, X. Wang, J. Li, Y. Wang, Q. Feng, Visible light photocatalytic property and mechanism

of peroxy bond incorporated layered $H_4Nb_6O_{17}$ niobate, J. Alloys Compd., 746 (2018) 68–76.
[38] F.D. Velázquez-Herrera, D. González-Rodal, G. Fetter, E. Pérez-Mayoral, Towards highly effect hydrotalcite/hydroxyapatite composites as novel catalysts involved in eco-synthesis of chromene derivatives, Appl. Clay Sci., 198 (2020) 105833, doi: 10.1016/j.clay.2020.105833.
[39] T.T.X. Hang, T.A. Truc, N.T. Duong, P.G. Vu, T. Hoang, Preparation and characterization of nanocontainers of corrosion inhibitor based on layered double hydroxides, Appl. Clay Sci., 67–68 (2012) 18–25.
[40] A.A. Dubale, I.N. Ahmed, Y. Zhang, X. Yang, M. Xie, A facile strategy for fabricating C@Cu_2O/CuO composite for efficient photochemical hydrogen production with high external quantum efficiency, Appl. Surf. Sci., 534 (2020) 147582, doi: 10.1016/j.apsusc.2020.147582.
[41] S.S. Kalanur, H. Seo, Facile growth of compositionally tuned copper vanadate nanostructured thin films for efficient photoelectrochemical water splitting, Appl. Catal., B, 249 (2019) 235–245.
[42] L. Kentjono, J.C. Liu, W.C. Chang, C. Irawan, Removal of boron and iodine from optoelectronic wastewater using Mg-Al (NO_3) layered double hydroxide, Desalination, 262 (2010) 280–283.
[43] Z. Yang, L. Zhang, P. Xu, X. Zhang, X. Niu, S. Zhou, The adsorption of nitrate from aqueous solution onto calcined Mg/Fe hydrotalcite, Desal. Water Treat., 54 (2015) 3400–3411.
[44] Q. Zhang, S. Wen, Q. Feng, S. Zhang, Surface characterization of azurite modified with sodium sulfide and its response to flotation mechanism, Sep. Purif. Technol., 242 (2020) 116760, doi: 10.1016/j.seppur.2020.116760.
[45] M. Testa, V.L. Parola, F. Mesrar, F. Ouanji, M. Kacimi, M. Ziyad, L. Liotta, Use of zirconium phosphate-sulphate as acid catalyst for synthesis of glycerol-based fuel additives, Catalysts, 9 (2019) 9020148, doi: 10.3390/catal9020148.

Supporting information

S1. Experiments

S1.1. Chemical reagents

Mg-Al hydrotalcite (HT) was purchased from Shaoyang Paradise Reagent, China. The Cu nitrate ($Cu(NO_3)_2{\cdot}3H_2O$, AR), absolute ethyl alcohol (CH_3CH_2OH, AR), sodium sulfide (Na_2S, AR), sodium hydroxide (NaOH, AR) and nitric acid (HNO_3, AR) were bought from Sinopharm Chemical Reagent Co., Ltd., China.

S1.2. Preparation of the adsorbents

3.00 g HT and $Cu(NO_3)_2{\cdot}3H_2O$ are uniformly dispersed in 60 mL mixture solution of alcohol and water with volume ratio of 1:1. The mixed system is stirred and evaporated at 95°C until the liquid evaporates completely. High temperature calcination at a heating rate of 5°C/min and a holding period of 180 min yielded the solid adsorbents CuO loaded hydrotalcite adsorbent (CuO-HT). CuO-loaded HT prepared by the different calcination temperature and different CuO loading amount is defined as CuO-HT-*x*-*y* (*x* = 0, 1, 2, 5, 10 mol.%; *y* = 100°C, 200°C, 300°C, 400°C, and 500°C).

S1.3. Characterization of the adsorbents

X-ray powder diffraction was carried out on a SmartLab SE X-ray Diffractometer (Rigaku Corporation, Japan) with Cu Kα radiation (λ = 0.15406 nm). The morphology and element distribution were observed by a scanning electron microscopy-mapping (SEM, FlexSEM 1000, Hitachi). The surface functional groups were investigated by Fourier-transform infrared spectroscopy (Nicolet iS50, Thermo Scientific, American) spectrometer. The Brunauer–Emmett–Teller specific surface area and Barrett–Joyner–Halenda pore-size distribution curves were obtained from N_2 adsorption–desorption isotherms determined at liquid nitrogen temperature (77 K) on a surface area and porosity analyzer (Micromeritics ASAP 2460, American). Samples were degassed at 473 K for 6 h prior to the measurement. The chemical composition and element valence were analyzed by an X-ray photoelectron spectroscopy (ESCALAB 250Xi, Thermo Scientific, American) with Al Kα radiation.

S1.4. Adsorption examination

50 mg of the as-prepared adsorbent was suspended into 100 mL of Na_2S solution (100 mg/L) and adjust pH = 10

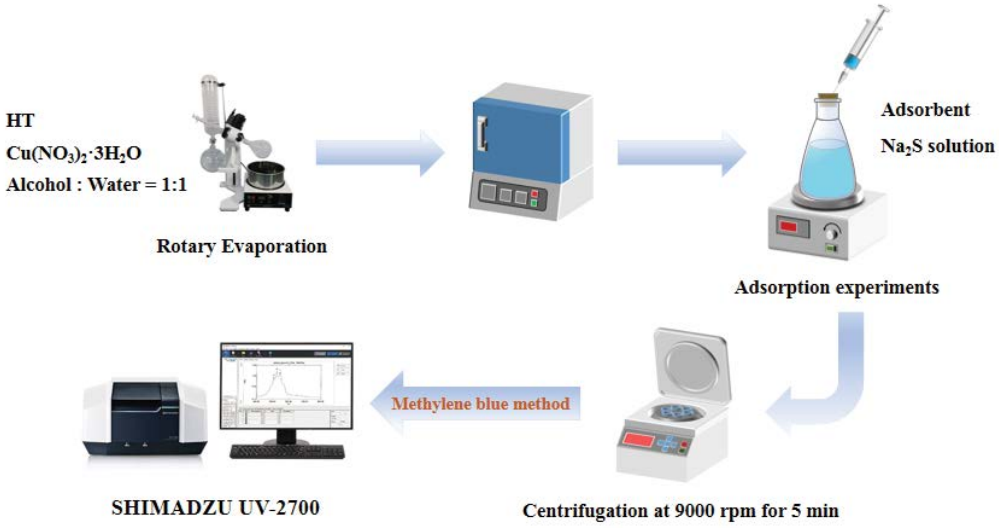

Fig. S1. Schematic illustration of the preparation and adsorption of the adsorbents.

with NaOH. It was held at room temperature for 80 min while being stirred in the dark. Nearly 3 mL of the suspension mixture was collected at 10 min intervals during stirring and separated by centrifugation at 9,000 rpm for 5 min. The concentration of Na_2S was analyzed with a Shimadzu UV-2700 Spectrophotometer (Japan) by methylene blue method. The schematic illustration of the preparation and adsorption of the adsorbents is showed in Fig. S1.

The sulfide adsorption performance is calculated as formula:

$$\eta = \frac{C_0 - C}{C_0} \times 100\% \quad (2)$$

where η is the sulfide adsorption accuracy, C_0 and C are the concentration of sulfide before and after adsorption (mg/L).

S1.5. Adsorbent regeneration

The regenerate procedure of the adsorbent was as follows. The worked adsorbent was washed in dilute nitric acid (pH = 6) for 3 times. The filtered solid adsorbent is washed, dried and calcined at 300°C for 3 h. The adsorption performance of the regenerated adsorbent was carried out under the same conditions as the as-prepared adsorbent.